3-D Reconstruction and Measurement of Microtubules from Multiple Angle-Total Internal Reflection Fluorescence Microscopy

Qian Yang Alexander Karpikov Derek Toomre James Duncan
Yale University
New Haven, CT, 06520
{qian.yang, alexander.karpikov, derek.toomre, james.duncan}@yale.edu

Abstract

Total internal reflection fluorescence (TIRF) microscopy excites a thin evanescent field which theoretically decays exponentially. Each TIRF image is actually the projection of a 3-D volume and hence cannot alone produce an accurate localization of structures in the z-dimension, however, it provides greatly improved axial resolution for biological samples. Multiple angle-TIRF microscopy allows controlled variation of the incident angle of the illuminating laser beam, thus generating a set of images of different penetration depths with the potential to reconstruct the 3-D volume of the sample. With the ultimate goal to quantify important biological parameters of microtubules, we present a method to reconstruct 3-D position and orientation of microtubules based on multi-angle TIRF data, as well as experimental calibration of the actual decay function of the evanescent field at each angle after taking into consideration the effect of point spread function, quantum efficiency and photon collection efficiency.

1. Introduction

The study of biological processes of cells and microtubules has been greatly aided by total internal reflection fluorescence (TIRF) microscopy. TIRFM exploits the unique properties of an induced evanescent wave field in a limited specimen region immediately adjacent to the interface between two media having different refractive indices. It can eliminate background fluorescence from outside the focal plane, thus, dramatically improve the signal-to-noise ratio, and consequently, the axial resolution of the features or events of interest. While the lateral resolution of TIRFM is about 150-200nm which is similar to confocal microscope, its axial resolution can be as high as 30-50nm.

Illumination of 3-D structures with fluorophore distribution $C(x, y, z)$ by an exponentially decaying evanescent field with decay constant $1/d$ will result in the intensity captured by the camera to be $C(x, y, z) \cdot \exp(-z/d)$. The final image detected by the objective lens will be an integral along the axial direction depending on the parameter d. By varying d, we are actually changing the angle of the incident laser beam leading to different projection images generated by the microscope.

The fluorophore distribution C(x,y,z) can be reconstructed using inverse Laplace transform with an accuracy of tens of nanometers. Ölveczky *et al*. [7] implemented it for a simple geometry and top-hat distribution of fluorohpore(either 0 or 1) to determine cell-substrate distances for the whole $x-y$ plane. More complex structures like spheres were modelled by Rohrbach[8] to reconstruct the diameters of isolated granules and the distance between vesicles in the solution and the coverslip. Reconstructions of more complicated 3-D structures have not been attempted to date.

A microtubule is a hollow cylinder, about 25nm in diameter and can be quite long(tens of microns). It has a plus end and a minus end, which make the microtubule dynamically unstable. Microtubules may grow steadily(polymerization) and shrink raplidly(depolymerization) at the plus end which we called a catastrophe. Microtubules have biomedical importance due to their functions as conveyer belts for vesicles inside the cell and to regulate cell migration and division.

The analysis of the dynamics and motion patterns of microtubules is difficult because the biological and mechanical mechanism that guides their behavior is still not very well known. Studies have shown that microtubules tend to bend when the tips touch a obstacle like a cell wall, or with contractile beating of heart cells[3]. When the curvature of the microtubule exceeds a certain threshold, it will break. There also have been some research on the motor complex that connects different microtubules. These motor proteins move from one end to the other on microtubules and cause crossing and twisting [5].

In this study we present a method based on a statistical framework to reconstruct 3-D curvilinear structures(e.g. microtubules) using optimization techniques. Instumentation was constructed to calibrate the axial profile of the

978-1-4244-3993-5/09/$25.00 ©2009 IEEE

TIRF microscope thus taking into consideration factors that make the profile deviate from theoretically predicted exponential. A maximum a posteriori framework was developed to compute the 3-D position and orientation along segmented microtubules. The method was validated using a computer generated phantom with known geometrical structure and fluorophore distributions, so we can apply it to multi-angle TIRF images of microtubules. (Fig.1) is an example of multi-angle TIRF images of microtubules with the penetration depths increase from top left to bottom right.

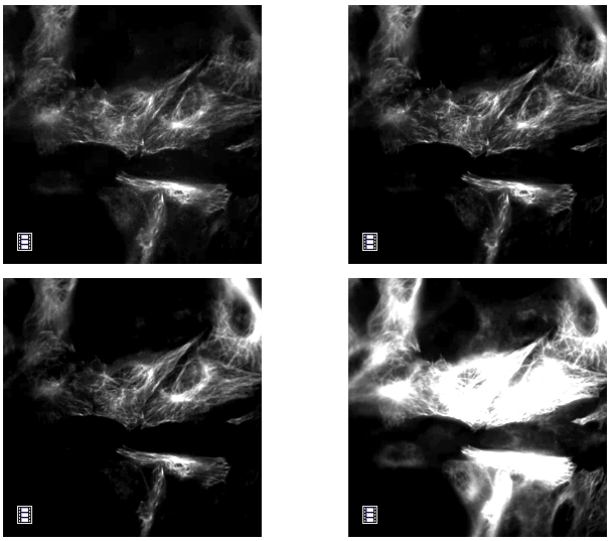

Figure 1. Multi-angle TIRF images. Top left: thinner penetration depth. Bottom right: deeper penetration depth

2. Methods

2.1. TIRF Imaging theory

An evanescent field is produced when the incident light beam traveling in a high refractive index medium (e.g. glass coverslip) reaches the interface with another low refractive index medium (e.g. oil, solution), if the incident angle is greater than the crtical angle. The critical angle θ_c is a function of the refractive indices of both media:

$$\theta_c = \sin^{-1}(n_i/n_t), \quad where \;\; n_i < n_t \tag{1}$$

Theoretically, the axial profile of the evanescent field behind the interface can be precisely described as following an exponential decay with a single parameter d, which refers to the penetration depth:

$$I(z, \theta_i) = I(0, \theta_i) \cdot e^{-z/d(\theta_i)} \tag{2}$$

The penetration depth d is associated with the incident angle:

$$d(\theta_i) = \lambda/4\pi \cdot (n_i^2 \cdot \sin^2\theta_i - n_t^2)^{-1/2} \tag{3}$$

where n is the refractive index and θ_i is the incident angle.

The intensity beyond the interface is represented as $I(x, y, z, d) = I_0(d) \cdot e^{-z/d}$, where $I_0(d) = I(z = 0, d(\theta_i))$ is the intensity directly behind the glass interface, which is given by Fresnel formulas[1]

$$I_0(\theta_i) = \frac{4\cos^2\theta_i(2\sin^2\theta_i - (n_t/n_i)^2)}{(n_t/n_i)^2\cos^2\theta_i + \sin^2\theta_i - (n_t/n_i)^2} \tag{4}$$

The following formula describes how a TIRF image is formed [8]:

$$\begin{aligned} &I(x, y, d) \\ &= \phi I_0(x, y, d) \int_0^\infty [Q(z)\mathrm{PSF}(z)]\, C(x, y, z) e^{-z/d} \mathrm{d}z \end{aligned} \tag{5}$$

Here I represents the multi-angle TIRF images we record, C is the actual fluorophore concentration in the volume, and I_0 is defined by (4). ϕ denotes the quantum efficiency of the fluorophores and CCD camera, $Q(z)$ and $PSF(z)$ are the collection efficiency and point spread function.

2.2. Challenges in Multi-angle TIRFM

Assuming a completely constant light source, the photon distribution over a set of bins of equal time is a Poisson probability distribution. Thus, the standard deviation of the number of photon N collected by the CCD camera is $\sqrt{N}$, therefore, the relative uncertainty is given by $\sqrt{N}/N = 1/\sqrt{N}$(Fig.2). This is the major factor leading to falling signal-to-noise ratio along axial direction as we increase the penetration depth to image a thicker part of the sample. Another important factor comes from the background fluorophore floating in the solution which will also be collected by the camera. Assuming an exponetial decay of the axial profile, we calculate the signal-to-noise ratio as a function of depth to be:

$$\begin{aligned} S/N &\propto \left[\frac{N}{\sqrt{N}}\right] \cdot \left[\frac{1}{\int_0^\infty e^{-z/d}\mathrm{d}z}\right] \\ &= \sqrt{N} \cdot \frac{1}{d} \\ &\propto \frac{e^{-z/2d}}{d} \end{aligned} \tag{6}$$

where the two terms in the right hand side brackets correspond to the shot noise(photon collecting process) and background fluorescence respectively.

This characterizes a major difference between multi-angle TIRF reconstruction from other reconstruction problems like tomography, where all images are projections of the entire volume and signal-to-noise ratio is the same. With multi-angle TIRFM, there will be a trade-off between the

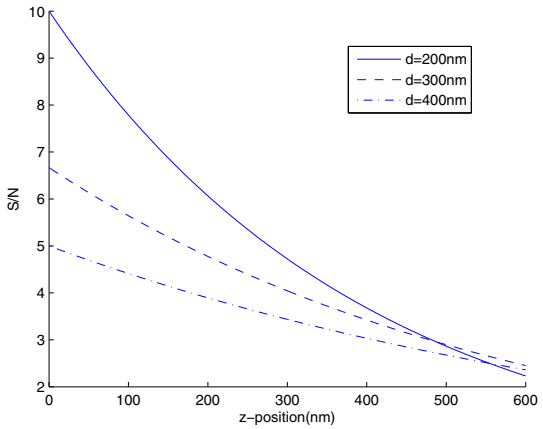

Figure 2. Shot noise/background fluorescence lead to decreasing S/N

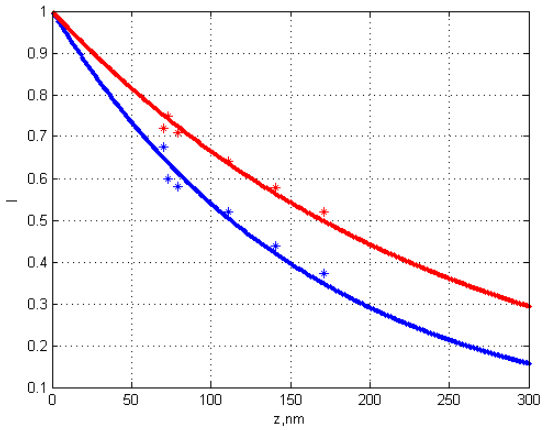

Figure 3. Intensity decay curves, blue line(lower one): penetration depth d=162 nm, red line(upper one): penetration depth d=245 nm. Stars-experimental points

amount of information and the S/N ratio, i.e. as you probe deeper into the sample with increasing penetration depth, S/N ratio will drop rapidly. So while it will be a good idea to use images with deep penetration depth as reference images for segmentation purposes, it will be necessary to revisit structures that also exist in low penetration depth images due to better S/N ratio .

2.3. Axial Profile Calibration

Ideally, when the penetration depth is shallow, we can assume the PSF to be constant[8]. However, in our multi-angle TIRF setup, the penetration depth varies from 80nm up to 700nm, which makes the actual profiles deviate considerably from a simple exponential.

An Objective-type TIRFM setup was used in our experiments to experimentally measure the actual decay profile. Total internal reflection was generated at the interface between the glass and the aqueous solution as a ring of laser light passes through the objective. We calibrated our TIRFM system by placing small beads (d=100nm) on the surface of a cell. Relative z positions of the beads were obtained by moving the microscope objective with 25nm steps and measuring the amount of blur as a function of z. By recording the position of the objective where the beads are sharpest(in focus), we generate an example of intensity decay curves: signal intensity as a function of z position of a bead is shown in (Fig.3)

Now with the calibrated axial decay profile $f(z,d)$, (5) simplies into:

$$I(x,y,d) = \int_0^\infty C(x,y,z)f(z,d)\mathrm{d}z \qquad (7)$$

2.4. MAP Framework with Neighbor Prior

To reconstruct microtubules of interest, we first segment them by manually selecting microtubule tips and finding the shortest path to cells or microtubule organizing centers[4]. We represent a microtubule centerline as $z(s)$, where s is the curve length. Let m be the number of points sampled along the microtubule, and n be the number of different angles we use to obtain TIRF images. We exclude points where microtubules cross each other where intensity will stack and cause confusion. Our goal now is to reconstruct the actual positions $[z_1, z_2, ..., z_m]$ from a set of TIRF images $[I_1, I_2, ..., I_n]$ corresponding to different penetration depths with axial decay profiles $[f_1, f_2, ..., f_n]$.

$$\begin{aligned}
z &= \arg\max_z p(z|I_1,...,I_n;f_1,...,f_n) \\
&= \arg\max_z \frac{p(I_1,...,I_n|z;f_1,...,f_n)p(z;f_1,...,f_n)}{p(I_1,...,I_n;f_1,...,f_n)} \\
&= \arg\max_z p(I_1,...,I_n|z;f_1,...,f_n)p(z) \\
&= \arg\max_z \left(\prod_{j=1}^{n} p(I_j(z)|f_j,z)\right)p(z) \\
&= \arg\max_z \left(\prod_{i=1}^{m}\prod_{j=1}^{n} \frac{f_j(z_i)^{I_j(z_i)}e^{-f_j(z_i)}}{I_j(z_i)!}\right)p(z)
\end{aligned} \qquad (8)$$

$p(I_j(z_i)|f_j,z_i)$ is the probability of getting projection image I_j given the microtubule's axial position z_i and the decay profile f_j corresponding to the current penetration depth d_j. It follws a poisson distribution which is given in (8). $p(I_1,...,I_n|z;f_1,...,f_n)$ is the joint density function of all sampled points along the segmented microtubule. Breaking up the joint density function into products of

$p(I_j(z_i)|f_j, z_i)$ is based on an assumption that assumes independence between projection images I_j correspondng to different penetration depths, which arises from independence between f's and z's. The former is an obvious result from the fact that f is solely dependent on the penetration depth, which are selected randomly by varying the incident angle. The independece of z's can be rationalized by the fact that the thickness of a reconstructed slice is much larger than the axial resolution of the microscope. Although local smoothness constraint applies to regulate neighboring z's, the dependence becomes much weaker when two points are separated due to thick slices.

2.5. MRF Neighbor Priors

The markov random field(MRF) is a common choice for prior models in image analysis when local smoothness constraint is applied[6] [2]. Markov random fields follow a Gibbs distribution:

$$p(z) = \frac{1}{X}\exp\left\{-\sum_{c\in\mathcal{C}} V_c(z_c)\right\} \tag{9}$$

X is the normalizing constant for the density known as the partition function. $\mathcal{C}$ is the set of all cliques(a clique is a set of points, c, which are all neighbors of each other. In the case of microtubules, each pair of neighboring points is a clique). $V_c(z_c)$ is the potential function of z_c.

We choose the potential function to be $|z_s - z_t|^\lambda$, where $\lambda \in (0, 2]$ is used to control the strength of the smoothness prior. $\lambda = 2$ is used in our actual computation.

$$p(z) = \frac{1}{X}\exp\left\{-\sum_{(s,t)\in\mathcal{C}} (z_s - z_t)^2\right\} \tag{10}$$

2.6. Energy Function of the Model

Combining the MRF prior into the MAP framework and take the logarithm, we can get the energy function of the model:

$$\begin{aligned} E(z) &= \log\left[\left(\prod_{i=1}^{m}\prod_{j=1}^{n}\frac{f_j(z_i)^{I_j(z_i)}e^{-f_j(z_i)}}{I_j(z_i)!}\right)p(z)\right] \\ &\propto \log\left[\left(\prod_{i=1}^{m}\prod_{j=1}^{n} f_j(z_i)^{I_j(z_i)}e^{-f_j(z_i)}\right)\right. \\ &\qquad \left.\cdot\exp\left(-\sum_{(s,t)\in\mathcal{C}}(z_s - z_t)^2\right)\right] \\ &= \sum_{i=1}^{m}\sum_{j=1}^{n}(I_j(z_i)\log(f_j(z_i)) - f_j(z_i)) \\ &\qquad -\sum_{(s,t)\in\mathcal{C}}(z_s - z_t)^2 \end{aligned} \tag{11}$$

Applying a gradient descent optimization(with step size α) to the energy function will lead to an iteration which will converge to the global maximum of $E(z)$.

$$\begin{aligned} z^{k+1} &= z^k + \alpha^k\cdot\nabla E(z) \\ &= z^k + \alpha^k\cdot\begin{pmatrix} \sum_j\left(\frac{I_j(z_1)}{f_j(z_1)} - 1\right)f_j'(z_1) \\ \sum_j\left(\frac{I_j(z_2)}{f_j(z_2)} - 1\right)f_j'(z_2) \\ \cdots \\ \sum_j\left(\frac{I_j(z_m)}{f_j(z_m)} - 1\right)f_j'(z_m) \end{pmatrix} \end{aligned} \tag{12}$$

3. Results

In our experiments we either generate TIRFM using a classic objective-type setup using a beam of light that is focused to a point on the outer back focal plane of a high numerical aperture (NA=1.495) oil-immersion lens (60X) or using custom optics generating a ring of light on the back focal plane of the objective. A ring of laser light passes through the microscope objective and undergoes total internal reflection at the interface between the glass and the aqueous solution. Totally internally reflected light penetrates the aqueous medium and forms evanescent waves which propagate parallel to the interface and exponentially decay in the direction normal to the interface. Fluorescent light excited by the evanescent waves is collected by the same objective. We change the penetration depth of the evanescent waves by changing the radius of the ring.

The typical penetration depth of a TIRF microscope is between $50nm$ to $1000nm$, which means anything deeper than $2000nm$ virtually has no effect on a TIRF projection image. To validate our method, we generated a computer simulated phantom data which is of size $20.48\mu m\times 20.48\mu m\times 2\mu m$, the volume is divided into $128\times128\times40$ voxels, meaning each voxel has a size of $160nm\times160nm\times50nm$, which corresponds to the resolution of the TIRF microscope. We put curvilinear structures in the volume and simulate the clustering and curving of microtubules, specifically, the shape of 5 microtubules coming out of an organizing center is constructed(white tubular structures in (Fig.4)).

The simulation process consists of two steps. First, we simulate the TIRF imaging process by projecting the volume into TIRF projection images using different decaying profiles, which correspond to different penetrations depths. Background noise is modeled as the ratio of fluorophore concentration in solution and on the object of interest, both are assumed to be uniform. Poisson distribution is used to model the photon collecting process of the CCD camera which generates a TIRF image. Both noise processes are tuned within a large range to test the robustness of the algorithm. Second, we use the set of projections images as

input to our method, and try to reconstruct the tubular objects. The red structures in (Fig.4) are our reconstruction results. Robustness is studied by plotting the graph of reconstruction error vs noise level(Fig.5) and reconstruction error vs depth of object of interest(Fig.6).

After the reconstructed axial position of the microtubules has been obtained, their orientation within the voxel can be determined by separately calculating the lateral orientation and axial tilting. Lateral orientation can be inferred from the Hessian matrix of the pixel in projection images[9], and axial tilting is the direct function of axial positions of neighboring sampled points along the microtubules.

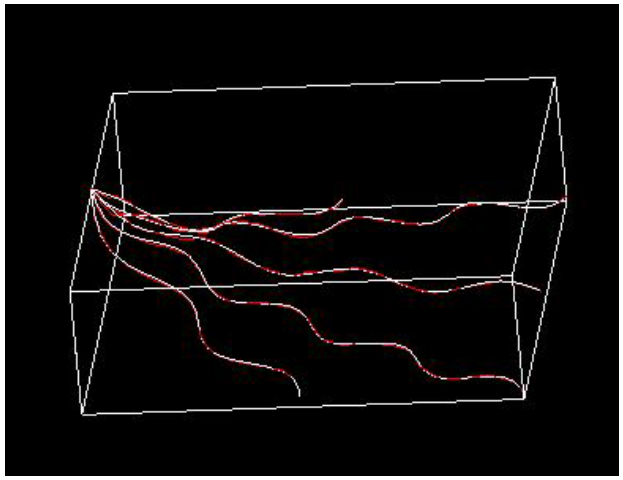

Figure 4. White: simulated phantom data, Red: reconstructed tubular structures

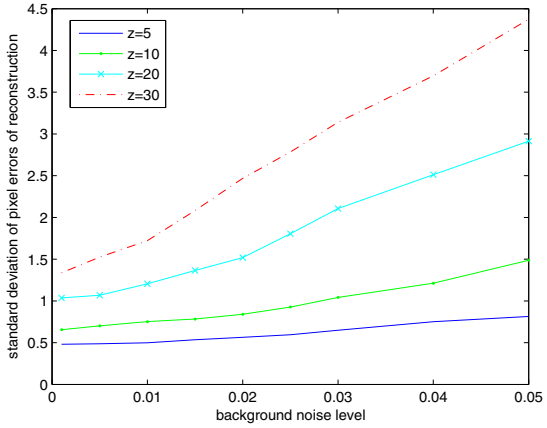

Figure 5. Reconstruction error vs background noise

4. Conclusion

The purpose of this study is to develop and validate a method based on MAP framework and optimization techniques to reconstruct 3-D structures from

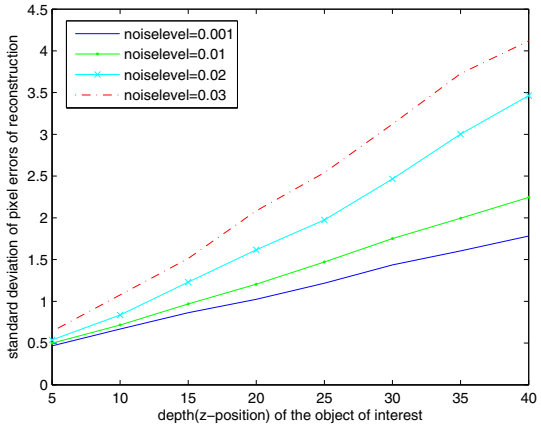

Figure 6. Reconstruction error vs depth of object of interest

a set of 2-D projection images generated using multi-angle TIRF microscopy. Since the exact value of incident angle/penetration depth is not available directly from objective-type TIRFM, we need to calibrate the multi-angle TIRFM instrumentation by experimentally measuring the axial decay profile of the evanescent field. The decay curves we measured can be fitted to an exponential decay to find the penetration depth. Our method takes the measured decay curves and corresponding projection images as input, and reconstructs the axial position of the objects of interest. By varying the noise level to test the robustness of the algorithm, we found that the reconstruction accuracy(represented by the standard deviation of the reconstuction error in pixels) is approximately linear versus the background noise level, which suggensts that our algorithm is quite robust to noise, especially when the structures being studied is close to the glass interface. While the structures of interest get deeper into the evanescent field, we would expect a linear deterioration of reconstruction accuracy. As suggested by (Fig.5) and (Fig.6), we conclude that our algorithm can correctly reconstruct 3-D structures, although with decreased accruracy when the noise level is high and the structures very deep.

The reconstruction method presented here will be useful for quantifying useful parameters related to microtubules' behavior(*e.g.* movement, growth, shrinking, etc.). The experiments and analysis here constitutes the preliminary stage of our ultimate goal to develop 3-D tracking algorithm to model and quantify important biological parameters, and we expect to obtain 3-4 multi-angle TIRF microtubules dataset sequences of living cells next month for reconstruction and tracking purposes.

References

[1] D. Axelrod, , E. H. Hellen, and R. M. fulbright. Total internal reflection fluorescence. *Topics in fluorescence spectroscopy: Principles and applications*, 3:289–343, 1992.

[2] C. Bouman, , and K. Sauer. A generalized gaussian image model for edge-preserving map estimation. *IEEE Transaction on Image Processing*, 2(3), 1993.

[3] C. P. Brangwynne, , F. C. MacKintosh, S. Kumar, N. A. Geisse, J. Talbot, L. Mahadevan, K. K. Parker, D. E. Ingber, and D. A. Weitz. Microtubules can bear enhanced compressive loads in living cells because of lateral reinforcement. *Journal of Cell Biology*, 173(5), 2006.

[4] L. D. Cohen, , and R. Kimmel. Global minium for active contour models: A minimum path approach. *International Journal of Computer Vision*, 24(1):57–78, 1997.

[5] F. cois N` edèlec. Computer simulations reveal motor properties generating stable antiparallel microtubule interactions. *Journal of Cell Biology*, 158(6), 2002.

[6] S. Geman, , and D. Geman. Stochastic relaxation, gibbs distributions, and the bayesian restoration of images. *IEEE Transaction on Pattern Analysis and Machine Intelligence*, 6(6), 1984.

[7] B. P. Ölveczky, , N. Periasamy, and A. S. Verkman. Mapping fluorophore distributions in three dimensions by quantitative multiple angle-total internal reflection fluorescence microscopy. *Biophysics Journal*, 73:2836–2847, 1997.

[8] A. Rohrbach. Observing secretory granules with a multiangle evanescent wave microscopy. *Biophysical Journal*, 78:2641–2654, 2000.

[9] Y. Sato, , S. Nakajima, N. Shiraga, H. Atsumi, S. Yoshida, T. Koller, G. Gerig, and R. Kikinis. 3-d multi-scale line filter for segmentation and visualization of curvilinear structures in medical images. *Medical Image Analysis*, 2(2), 1998.